Effects of cylinder Reynolds number on the turbulent horseshoe vortex system and near wake of a surface-mounted circular cylinder

Gokhan Kirkil, and George Constantinescu

View Online   Export Citation   CrossMark

ARTICLES YOU MAY BE INTERESTED IN

AIP Author Services
English Language Editing

AIP Publishing

Effects of cylinder Reynolds number on the turbulent horseshoe vortex system and near wake of a surface-mounted circular cylinder

Gokhan Kirkil[a)] and George Constantinescu
Department of Civil and Environmental Engineering, IIHR-Hydroscience and Engineering, The University of Iowa, Iowa City, Iowa 52242, USA

The turbulent horseshoe vortex (HV) system and the near-wake flow past a circular cylinder mounted on a flat bed in an open channel are investigated based on the results of eddy-resolving simulations and supporting flow visualizations. Of particular interest are the changes in the mean flow and turbulence statistics within the HV region as the necklace vortices wrap around the cylinder's base and the variation of the mean flow and turbulence statistics in the near wake, in between the channel bed and the free surface. While it is well known that the drag crisis induces important changes in the flow past infinitely long circular cylinders, the changes are less understood and more complex for the case of flow past a surface-mounted cylinder. This is because even at very high cylinder Reynolds numbers, Re_D, the flow regime remains subcritical in the vicinity of the bed surface due to the reduction of the incoming flow velocity within the bottom boundary layer. The paper provides a detailed discussion of the changes in the flow physics between cylinder Reynolds numbers at which the flow in the upstream part of the separated shear layers (SSLs) is laminar ($Re_D = 16\,000$, subcritical flow regime) and Reynolds numbers at which the transition occurs inside the attached boundary layers away from the bed and the flow within the SSLs is turbulent ($Re_D = 5 * 10^5$, supercritical flow regime). The changes between the two regimes in the dynamics and level of coherence of the large-scale coherent structures (necklace vortices, vortex tubes shed in the SSLs and roller vortices shed in the wake) and their capacity to induce high-magnitude bed friction velocities in the mean and instantaneous flow fields and to amplify the near-bed turbulence are analyzed. Being able to quantitatively and qualitatively describe these changes is critical to understand Reynolds-number-induced scale effects on sediment erosion mechanisms around cylinders mounted on a loose bed, which is a problem of great practical relevance (e.g., for pier scour studies). © *2015 AIP Publishing LLC.*
[http://dx.doi.org/10.1063/1.4923063]

I. INTRODUCTION

Compared to the flow past an infinitively long circular cylinder (Williamson[1]), the flow past a surface-mounted circular cylinder placed in a channel is more complex due to the effects of the channel bottom and free surface. As for any junction flow past a bluff body, the combined effect of the no slip bottom boundary and strong deceleration of the flow as it approaches the cylinder induces a downflow parallel to the leading face of the cylinder, the separation of the incoming bottom boundary layer and the formation of a horseshoe vortex (HV) system containing necklace vortices.[2–4] The downflow feeds fluid originating away from the channel bottom into the HV system. The necklace vortices are stretched as they wrap around the leading face of the cylinder and their legs bend to become close to parallel to the incoming mean flow direction.

---

a)Present address: Department of Energy Systems Engineering, Kadir Has University, Istanbul 34083, Turkey.

A laminar or turbulent HV system is observed depending on the nature of the incoming bottom boundary layer at the location of the cylinder.[5–12] Most experimental studies (e.g., Wei *et al.*, 2001[12]) observed transition from a laminar to a turbulent HV system to occur at cylinder Reynolds numbers (Re_D) defined with the incoming depth-averaged mean flow velocity, U, and maximum width/diameter of the cylinder, D, between 10 000 and 18 000. In the case of a turbulent HV system, the location, size, and level of coherence of the necklace vortices are highly variable in time and a high amplification of the turbulence is observed within the HV region.[2,11] Experimental investigations[2,8,12,14–19] have increased considerably our understanding of the intricate structure of the turbulent HV system forming around surface-mounted bluff-body cylinders, especially in the symmetry plane.

Other effects due to the finite flow depth include oblique shedding of the vortex tubes in the separated shear layers (SSLs), the formation of large-scale vortical eddies behind the cylinder, the strong damping of the normal velocity fluctuations in the vicinity of the two boundaries, and significant vertical mean flow motions in the near-wake region. Flow nonuniformity in the vertical direction is particularly large for relatively shallow cases (low ratio between the flow depth, H, and the cylinder diameter, D). Moreover, the coherence of the roller vortices is not uniform along the vertical direction due to the loss in coherence as these vortices interact with the bed surface and near bed turbulence. A non-negligible upward oriented axial flow is observed inside the core of roller vortices shed behind a surface-mounted cylinder in a relatively shallow channel.[20] Thus, the roller vortices shed behind finite-length cylinders are not exactly similar to the ones observed past long cylinders even if Re_D is the same.[21,22]

In most practical applications where cylinder-like obstructions (e.g., bridge piers and other types of hydraulic and coastal structures, flow past islands) are placed on a loose bed, the incoming flow is fully turbulent and the cylinder Reynolds number, Re_D, is sufficiently high for a turbulent HV system to form. Moreover, Re_D is typically higher than the threshold value above which the drag crisis occurs on the cylinder (e.g., $Re_D \cong 3 * 10^5$ for circular cylinders). Sediment entrainment and scour around cylinders placed on a loose bed are driven by the energetically important coherent structures in the flow and in particular by the necklace vortices.[23–25] Though the structure and dynamics of the turbulent HV system in the symmetry plane of cylinders of different shapes were investigated in detail (e.g., see Simpson,[11] for a review), the dynamics and structure of the necklace vortices as they wrap around the cylinder and of their legs are less understood, but critically important to evaluate the sediment entrainment capacity of the flow.

Most previous experimental investigations of flow past surface-mounted cylinders provide measurements of the mean velocity and Reynolds stresses in selected 2D sections and dye visualizations of the vortices. As already mentioned, most of the investigations that focused on the turbulent HV system generally provide such measurements only in the symmetry plane of the cylinder,[8,25] while those focusing on the general flow structure (e.g., Graf and Yulistiyanto,[26] for a circular cylinder placed in a deep open channel at $Re_D \cong 10^5$) provide measurements in several vertical planes but do not provide a detailed description of the flow in the small region containing the HV system. Other experiments focused on the structure of the near wake flow.[20,27] The flow past the cylinder in these experimental investigations was subcritical.

Fine-resolution eddy-resolving simulations provide the entire 3-D instantaneous flow fields and allow estimating the boundary stresses in the instantaneous and mean flow fields. Such simulations can supplement the information usually available from experimental studies and provide a more detailed and accurate description of the dynamics of the energetically important coherent structures (e.g., of the necklace vortices, see Simpson[11]) and of their capacity to induce bed erosion in the case of a loose bed. This approach was successfully used to investigate flow past cylinders of various shapes mounted on a flat[28,29] or deformed bed[30] and, in particular, the dynamics of the HV system.

In the present study, we discuss the physics of flow past a circular cylinder placed in a relatively shallow open channel (H/D = 1.12) based primarily on results of eddy-resolving simulations. As the incoming flow is fully turbulent and the ratio H/D is larger than 0.8 such that the interactions between the HV system and the free surface are negligible, the structure of the flow around the cylinder is mainly a function of Re_D. In all test cases reported in this paper, Re_D is sufficiently high such that a turbulent HV system is observed. In this regard, the present work is directly related to

a previous study from our group (Kirkil and Constantinescu[31]) conducted for the same geometrical configuration but with $Re_D < 5000$ for which a laminar HV system was observed. Understanding the physics of high Re_D flow past circular cylinders is also directly relevant for understanding flow, turbulence structure, and sediment entrainment mechanisms around cylindrical obstructions whose cross section contains no sharp edges, for which the position of the separation line on the cylinder is dictated by the flow. As Re_D is increased (e.g., from 16 000 to $5 * 10^5$) and the drag crisis occurs, the position of the separation line moves downstream (e.g., the polar angle at which separation occurs, ϕ_s, and increases from 90° to about 110° for long cylinders). The case of a circular cylinder is different from the case of cylinders whose cross section contains sharp edges (e.g., rectangular cylinders and plates), where the positions of the separation lines coincide with the sharp edges of the cylinder and are independent of Re_D (Chang *et al.*[29]). In the present study, we consider cases in which the wake stability number is sufficiently small such that the vortex shedding mode is observed. Thus, the shallow turbulent wake contains roller vortices that are similar to those present in the von Karman vortex street observed behind infinitely long cylinders.

The main research questions we try to answer are as follows:

- How do the flow and turbulence structure inside the turbulent HV system forming at the base of a circular cylinder vary with the polar angle?
- How do the mean flow and turbulence structure of the near wake change over the flow depth?
- What are the main changes in the dynamics of the HV system and the characteristics of the large-scale shedding behind the cylinder as Re_D increases and the drag crisis occurs? How do these changes affect the mean flow and turbulence statistics?
- What are the main sediment erosion mechanisms around circular cylinders mounted on a loose bed at conditions corresponding to the start of the local scour process (flat channel bed)? How does the potential of the flow to erode the bed change with the increase of Re_D? This is an important question because most of the detailed experimental studies of local scour around surface-mounted circular cylinders were conducted at relatively low Re_D (subcritical flow regime). The present study should provide a better understanding of the extent to which results based on scaled-model laboratory studies can be extrapolated for practical applications where the flow regime past the cylinder is supercritical.

II. DESCRIPTION OF THE NUMERICAL AND EXPERIMENTAL METHODOLOGIES AND TEST CASES

A. Numerical model

The viscous flow solver employed in this work is the same as the one used in the companion paper by Kirkil and Constantinescu[31] that investigated flow past a cylinder placed in an open channel at low Reynolds numbers ($Re_D < 5000$). The reader is referred to that paper for a more detailed description of the collocated finite-volume scheme used to solve the filtered Navier-Stokes equations (see also Mahesh *et al.*[32]). The fractional step algorithm is second-order accurate in both space and time. Similar to the simulations reported in Kirkil and Constantinescu,[31] the free surface is treated as a rigid lid, symmetry boundary conditions are used at the lateral boundaries, and no slip conditions are imposed on the cylinder surface and at the bed. A convective boundary condition is used at the outflow boundary. The main difference is the treatment of the inflow conditions. Frohlich and von Terzi[33] provide a detailed discussion of the advantages of specifying unsteady boundary conditions at the inlet boundary in eddy resolving simulations that mimic as closely as possible realistic turbulent flow fields. In the present work, precursor eddy resolving simulations in a straight channel with periodic boundary conditions in the streamwise direction were conducted to generate flow fields containing realistic turbulence fluctuations corresponding to fully developed open channel flow. The channel cross section and the channel Reynolds numbers were identical in the simulations containing the cylinder and the corresponding precursor simulations. These instantaneous flow fields were then fed in a time accurate way through the inflow section of the computational domain containing the cylinder. The mean streamwise velocity profile in the vertical direction in
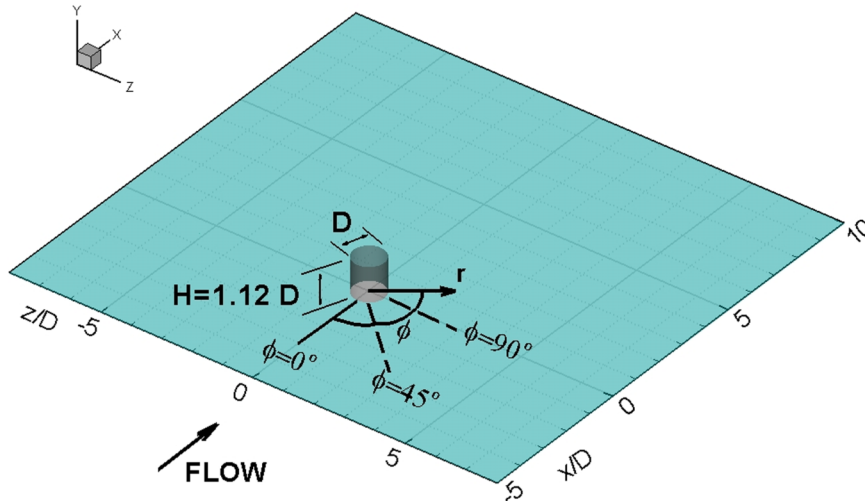
FIG. 1. Sketch showing computational domain and definition of polar angle. The cylinder's face corresponds to r = 0.5D.

the inflow section calculated from the precursor simulations followed the standard log-law variation away from the channel bottom.

B. Simulations setup, boundary conditions, and computational meshes

The channel depth was H = 1.12D, same as the one in the simulations discussed by Kirkil and Constantinescu.[31] The computational domain extended 5D upstream and 10D downstream of the cylinder. The lateral extent of the domain was 16D. The origin of the system of coordinates was located at the center of the cylinder on the bottom surface, with the x axis corresponding to the streamwise direction and the y axis to the vertical direction. The polar angle, ϕ, is equal to zero in the upstream symmetry plane of the cylinder (Fig. 1). No wall functions were used. The governing equations were integrated through the viscous sub-layer, which allowed estimating the boundary stresses without relaying on the logarithmic law-of-the-wall assumption. In both simulations, the mesh was refined in the wall normal direction. The first point of the solid surfaces was placed at less than 1.5 nondimensional wall units from the solid surface, where the nondimensional wall units corresponding to a distance n from the closest solid surface, $n^+ = nu_{\tau 0}/\nu$, are defined with the mean bed friction velocity in the incoming channel, $u_{\tau 0}$, and the molecular viscosity, ν.

The code was run until the flow became statistically steady, after which instantaneous flow fields were collected over 80D/U and used to calculate statistics. The statistics were checked for convergence. The modeled contribution to the total (modeled plus resolved) Reynolds stresses was, in average, less than 20% in case LR and less than 30% in case HR in the regions containing the HV, the SSLs, and the near wake, up to x/D = 2.0.

The low Reynolds number simulation (case LR) was performed with Re_D = 16 000. The mesh contained over 4×10^6 cells. The time step was 0.002D/U. The maximum Courant number was close to 0.3. The dynamic Smagorinsky model was used to account for the effect of subgrid-scale motions on the resolved velocity field. Typical computational cell dimensions inside the HV system and SSLs were 4–25 nondimensional wall units, which is more than sufficient to accurately capture the dynamically important eddies that populate these regions. Kirkil and Constantinescu[31] provide more details on the computational mesh used in the LR simulation. They also discuss additional validation studies conducted for flow past long cylinders (see also Mahesh et al.[32]) and for flow past surface-mounted bluff bodies placed in a straight channel at comparable Reynolds numbers.[30,36,37]

The high Reynolds number simulation (case HR) was performed with $Re_D = 5 * 10^5$. Because of the much higher Reynolds number, detached eddy simulation (DES) was used to account for the effect of the unresolved scales. The Spalart-Allmaras version of the DES model[38] was used to conduct the HR simulation. Its implementation is similar to the one described in Chang et al.[40]

Similar to the Smagorinsky model, DES predicts an eddy viscosity proportional to the square of the average cell size away from the solid surfaces. DES was shown to be more accurate than Large Eddy Simulation (LES) with wall functions for predicting complex flow in channels provided that the incoming flow contains realistic turbulent fluctuations.[39]

It is also relevant to mention that DES with steady inflow conditions conducted by Paik *et al.*[28] for flow past a winged-shaped cylinder was not able to correctly predict the location of the primary necklace vortex in the mean flow and the regions of high amplification of the turbulent kinetic energy (tke) and turbulence production relative to the cylinder, despite being able to correctly capture most of the other features of the flow and turbulence structure within the HV system revealed by the experimental investigation of Devenport and Simpson.[8] Simulations conducted in our group (e.g., see Chang *et al.*[40]), including the ones performed as part of the present study, have shown that the predictive capabilities of DES improve significantly when such simulations are conducted with unsteady inflow flow fields containing realistic turbulent fluctuations. These conditions also mimic the ones typically observed in long natural open channels containing flow obstructions. Moreover, a preliminary DES simulation of case LR conducted with realistic turbulent fluctuations obtained from a precursor simulation showed that the mean flow and turbulence statistics predicted by DES were very close to those obtained in the LR simulation using the dynamic Smagorinsky model.

The mesh in the simulation of case HR contained around 8.5×10^6 cells, with about 70 grid points used to resolve the flow in the vertical direction. This larger number of grid points was needed to sufficiently resolve the attached boundary layers in the wall-normal direction on the no-slip surfaces and the energetically important eddies in the flow whose mean size (e.g., average diameters of the cores of vortex tubes in the SSLs and necklace vortices) decreases with the increase in Re_D. Though the resolution in terms of nondimensional wall units was less than the one for case LR, the average number of grid points used to resolve the HV system and the SSLs was about the same. This resolution is comparable to the one used in other DES of flow past surface mounted bodies at comparable Reynolds numbers.[29] The core of the primary necklace vortex and the vortex tubes was situated in the region where the LES mode of DES was active. The mesh spacing was such that the switch to the LES mode occurred at around 0.02-0.04D from the solid surfaces. The time step was 0.0025D/U.

In both cases, the mesh resolution was such that 6-8 grid points were placed across the SSLs. The maximum grid spacing in the vertical direction was 0.04D close to the free surface. The cell size in the radial direction was around 0.02-0.05D within the HV region. The cell sizes in the vertical and polar directions within the same region were around 0.01D and 0.02D, respectively. The core of the primary necklace vortex was resolved with at least 6 points. This mesh point distribution insured a low aspect ratio for most of the cells situated within the HV region and the SSLs away from the channel bed and the cylinder surface. Close to those surfaces, the aspect ratios were much higher (e.g., up to 30) due to the need to resolve the attached boundary layers in the wall normal direction.

C. Experiments

As part of the present study, Large Scale Particle Image Velocimetry (LSPIV) was used to visualize the mean flow patterns at the free surface and to estimate the size of the recirculation regions.[34] Details of the LSPIV technique and the image processing algorithms used in the present study are given by Fujita *et al.*[34] The same LSPIV technique was already applied by our group to characterize the mean free surface flow around surface-mounted emerged cylinders with flat bed and equilibrium scour bed (Ettema *et al.*,[13] Kirkil *et al.*[30]) and around vertical-wall obstructions mounted at the sidewall of an open channel (Koken and Constantinescu[36]).

Experiments were conducted with H/D = 1.12 and Re_D corresponding to cases LR and HR. In both cases, the circular cylinder was placed at the centerline of the flume, far from the inflow section to ensure that the flow was fully developed before it reached the cylinder. Saw dust floating particles were used to seed the flow at the free surface. The saw dust particles were fed continuously upstream of the cylinder in a uniform fashion throughout the flume width. Image recording was done by means of a digital video camera (Sony TVR-320) that produced geometrically non-distorted

images. The camera was mounted at a height of 1 m above the water surface. The digitized images contained 640×480 pixels of 8-bit, gray-level resolution. Image processing was performed using a commercial software LSIV v.5.0 that allows calculation of the mean velocities and 2-D streamlines. The uncertainty in the estimation of the mean velocity field by the present LSPIV technique is spatially distributed and is in the range of 2%-8% (Muste et al.[35]).

The experiments corresponding to case LR were conducted in a 27.4 m long, 0.91 m wide, and 0.45 m deep tilting flume with a flow depth H = 0.1 m (D = 0.09 m) and a mean velocity, U = 0.18 m/s. The experiments corresponding to case HR were conducted in a 20 m long, 3 m wide, and 1.5 m deep flume with H = 0.53 m (D = 0.47 m) and U = 0.9 m/s. More details on the flumes in which the experiments were performed and the experiment setup is given in Kirkil et al.[30] and Kirkil.[41] In all experiments, the deformations of the free surface were relatively small (less than 0.03D).

III. HORSESHOE VORTEX SYSTEM

A. Flow structure in the HV region and dynamics of necklace vortices

Figure 2(a) shows the structure of HV system in the mean flow for case LR. The Q criterion[42] is used to visualize the necklace vortices, where Q is the second invariant of the velocity gradient tensor. Besides the primary necklace vortex, PV, a small corner vortex, CV, is present near the junction line between the upstream face of the cylinder and the bed. No secondary necklace vortices are present in the mean flow. The structure of the flow within the HV region in case HR is qualitatively very similar to that discussed for case LR.

Additional analysis of the flow fields shows that the circulation of PV is the largest in the symmetry plane, $\phi = 0°$, and decreases monotonically with $|\phi|$ (not shown). This trend is consistent with the monotonic decay of the cross section of PV with $|\phi|$ observed in Fig. 2(a), where PV is visualized using a Q = constant isosurface. As Re_D increases, the nondimensional circulation of PV is increasing significantly in $|\phi|$ = constant planes (by close to 100% between cases LR and HR) and its rate of decay with $|\phi|$ is smaller, at least until $|\phi| = 60°$. Moreover, the axis of PV moves closer to the bed with increasing Re_D.

Examination of the instantaneous flow fields for cases LR and HR shows that besides the primary necklace vortex, PV, a variable number of smaller secondary necklace vortices are present inside the HV region. Once a new secondary necklace vortex detaches from the region where the incoming boundary layer separates, it is advected toward the PV. This is similar to what was observed by Kim et al.[44] based on visualizations of the flow in the symmetry plane of a cylinder. The degree of coherence of PV, measured by the circulation along the polar direction in planes perpendicular to its axis, and the distance between PV and the junction line were found to be subject to large variations in time and along the axis of PV (e.g., in the polar direction). The main trends are illustrated for case LR in Figs. 2(b) and 2(c) that visualize the core of PV at two time instances, when PV is situated at a large distance from the cylinder and when PV is situated very close to the junction line. The core of the vortex is larger when PV is located away from the junction line. In
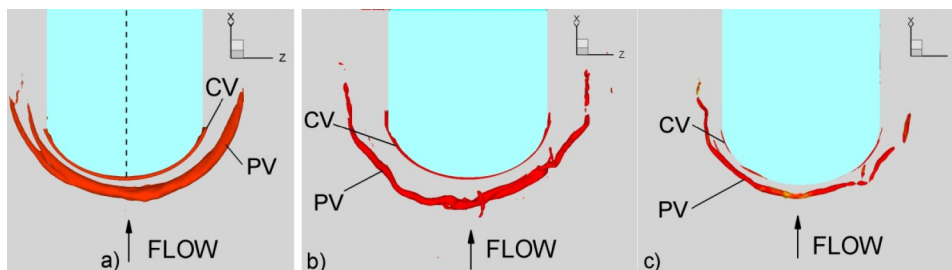

FIG. 2. Visualization of the HV system (case LR) using a Q isosurface (Q = 2). (a) Mean flow; (b) instantaneous flow when the primary necklace vortex PV is situated away from the cylinder; (c) instantaneous flow when the primary necklace vortex PV is situated close to the cylinder.

the flow field of Fig. 2(b), the coherence of PV is larger on the right side of the cylinder, while the opposite is true in Fig. 2(c). The main mechanism for the increase of the coherence of PV, especially for low |φ|'s, where the adverse pressure gradients close to the cylinder face are high, is the advection of vortical eddies originating in the downflow toward PV after these eddies reach the channel bed.[2,24,29] Examination of the instantaneous flow fields showed that another mechanism responsible for the local increase of the coherence of PV, especially for high |φ|'s, is the merging and extraction of vorticity of same sign from the core of a secondary necklace vortex. These mechanisms are essentially the same for cases LR and HR.

B. Bimodal oscillations

A fundamental question related to flow structure inside the HV region is what is the reason why necklace vortices forming at the base of a bluff body are so efficient in entraining sediment from a loose bed? Visualizations of PV in case LR (Figs. 2(b) and 2(c)) have already shown that the position and size of PV are subject to large temporal variations. As the analysis below will show and consistent with results of previous investigations of junction flows where a turbulent HV system is forming,[11] the PV was found to be subject to large-scale aperiodic bimodal oscillations in both cases. The oscillations take place between a zero-flow mode, where PV is situated close to the cylinder and the shape of its core is close to circular, and a back flow mode, where PV is situated away from the cylinder, the size of its core is larger and the shape of its core is close to an ellipsoid. The frames in Fig. 3 illustrate the transition of PV from the back flow mode to the zero flow mode in the symmetry plane of the cylinder for case LR. Figure 4 shows the HV region in case HR at two time instances, when PV is in the zero flow mode and in the back flow mode.

Of critical importance for sediment entrainment are the sweeping motions of the core of PV as it oscillates between the two modes and the near-bed jet-like flow forming beneath PV. The intensity of the reversed jet-like flow is modulated by injection of vortical eddies from the downflow into PV.[2,8,36] The streamwise extent of the jet-like flow peaks when PV is in the back flow mode. For case LR, the average distance between the separation line and the cylinder's face in the symmetry plane is 0.35D when PV is in the back flow mode and 0.15D when PV is in the zero flow mode. A weak recirculation region is present upstream of the separation line (Fig. 3), which is consistent with the experiments of Devenport and Simpson.[8] The size of the recirculation region peaks during the time PV is in the zero-flow mode. The structure of the flow within the HV region is qualitatively
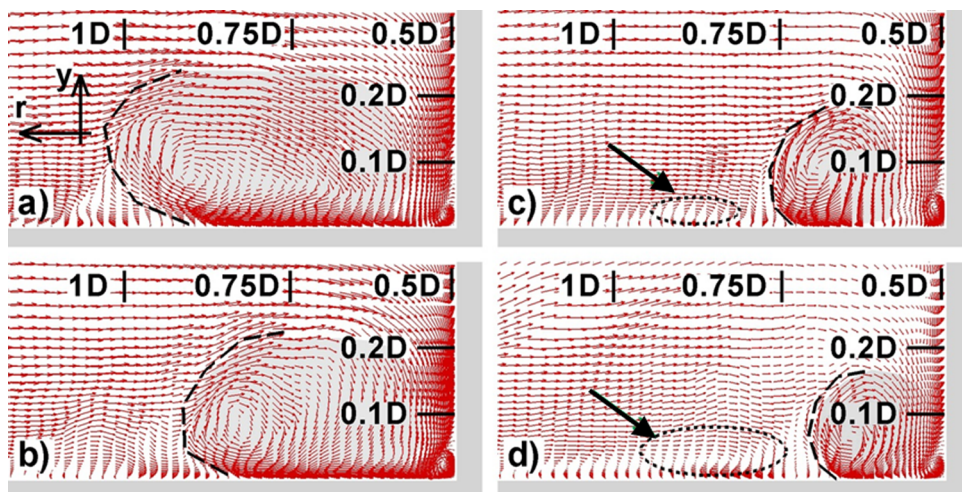

FIG. 3. Visualization of the HV system transitioning from the back flow mode (frame (a)) to the zero flow mode (frame (d)) in the φ = 0° plane for case LR. The arrow points toward a recirculation region forming in front of the primary necklace vortex PV. The upstream face of the cylinder is situated at r = 0.5D.
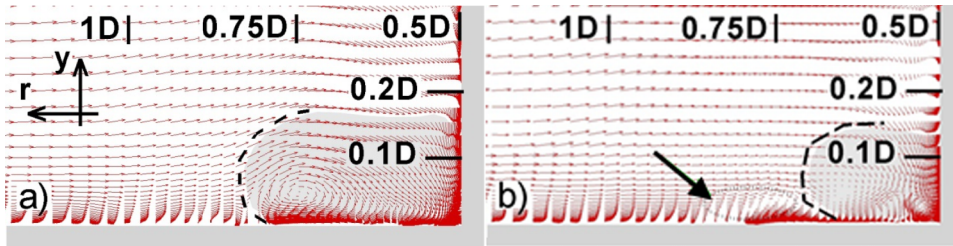
FIG. 4. Visualization of the HV system in the back flow mode (frame (a)) and in the zero flow mode (frame (b)) in the $\phi = 0°$ plane for case HR. The arrow points toward a recirculation region forming in front of the primary necklace vortex PV. The upstream face of the cylinder is situated at $r = 0.5D$.

similar for case HR (Fig. 4), though the mean amplitude of the bimodal oscillations in the radial direction and the size of the core of PV in the back flow mode are smaller compared to case LR.

Analysis of the instantaneous flow fields for cases LR and HR showed that the transition to the back flow mode is primarily triggered by the entrainment of patches of high-momentum fluid from the incoming fully developed flow first into the downflow and then into the HV region. As such an event occurs, the jet-like flow beneath the HV region increases its momentum and forces PV to move away from the cylinder. Once in the back flow mode, the large but not very coherent necklace vortex system gets stretched around the cylinder and its cross section gets smaller. Meanwhile, the intensity of the jet-like flow decreases if no new patches or high-momentum fluid are injected from the downflow. As a result, PV moves closer to the cylinder (transition to the zero flow mode). Two main mechanisms can result in a significant increase of the coherence of PV as it transitions toward the zero flow mode. The first one, also discussed by Devenport and Simpson,[8] is the injection of patches of high-vorticity low-momentum fluid from the downflow inside the HV region. The second one, which is important especially at high $|\phi|$'s, is the merging of PV with secondary co-rotating necklace vortices advected toward the cylinder.

C. Turbulence structure

1. Turbulent kinetic energy and Reynolds stresses

An important consequence of the bimodal oscillations of PV is the large amplification of the turbulence within the HV region.[45] The experiments of Devenport and Simpson[8] conducted for a wing-body cylinder at a Reynolds number defined with the width of the cylinder of 125 000 and an incoming developing turbulent boundary layer have shown that the level of turbulence amplification of the Reynolds stresses within the HV region is about one order of magnitude larger than the one observed in the incoming turbulent boundary layer. Present results for cases LR and HR show that this is also the case for circular cylinders placed in a fully developed turbulent incoming flow. For example, the peak values of the tke in the $\phi = 0°$ and $\phi = 45°$ polar sections in Figs. 5 and 6 (the regions of low magnitude of $\overline{v'v'}$ and tke were blanked out) are close to 15 and, respectively, 9 times higher than the mean values in the incoming fully developed channel flow for cases LR and HR, respectively. The mean values of the tke in the incoming flow are close to $0.0034U^2$ in the LR and HR simulations. The position of the patch of high tke in the three sections approximately corresponds to the core of PV in the mean flow (not shown).

A detailed analysis of the turbulence statistics in different polar sections confirmed that the peak intensities of the tke (Fig. 6), the mean velocity fluctuations in the vertical direction (Fig. 5), and in the radial direction (not shown) decay monotonically with $|\phi|$ in case LR. A decay of k/U^2 and $\overline{v'v'}/U^2$ with $|\phi|$ is also observed for $|\phi| > 45°$ in case HR (Figs. 5(b) and 5(c), 6(b) and 6(c)). However, for case HR, the peak values of k/U^2 and $\overline{v'v'}/U^2$ are slightly increasing with the polar angle for $|\phi| < 45°$ (Figs. 5(a) and 5(b), 6(a) and 6(b)). As explained next, this is mostly because of the larger energy content of the eddies advected from the downflow into the HV region.

Additional analysis of the instantaneous flow fields showed that the presence of strongly energetic eddies within the downflow is the main reason why the nondimensional levels of the mean
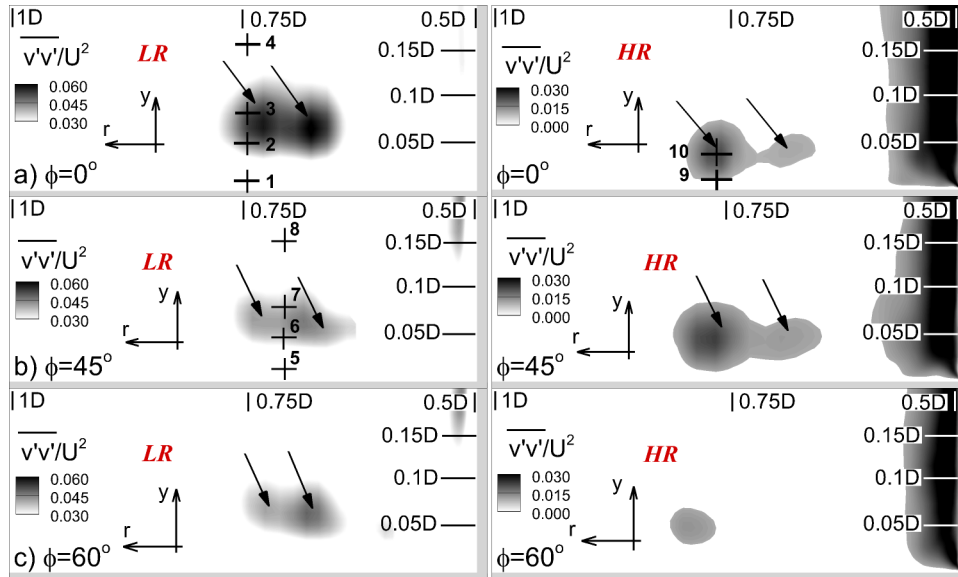
FIG. 5. Mean turbulent velocity fluctuations in the vertical direction, $\overline{v'v'}/U^2$, in case LR (left) and case HR. (a) $\phi = 0°$; (b) $\phi = 45°$; (c) $\phi = 60°$ plane. The upstream face of the cylinder is situated at $r = 0.5D$. Values of $\overline{v'v'}/U^2$ less than 0.03 for case LR and less than 0.01 for case HR were blanked out.

vertical velocity fluctuations within the downflow (e.g., the peak levels of $\overline{v'v'}/U^2$ inside the downflow are 0.03-0.04 for $|\phi| < 60°$ in case LR and 0.05-0.06 in case HR) and of the mean radial velocity fluctuations within the jet-like flow are larger in case HR. As a result, the tke levels within these two regions are larger in case HR compared to case LR. For example, in the $|\phi| = 0°$ and $45°$ sections, the peak values of k/U^2 within the jet-like flow are close to 0.04 in case HR and 0.02-0.03 in case LR (not shown). This happens despite the fact that the peak tke values within the core of PV are larger in case LR than in case HR (Figs. 6(a) and 6(b)). The injection of energetic eddies into the core of PV results in vertical and lateral oscillations of the axis of the vortex. As
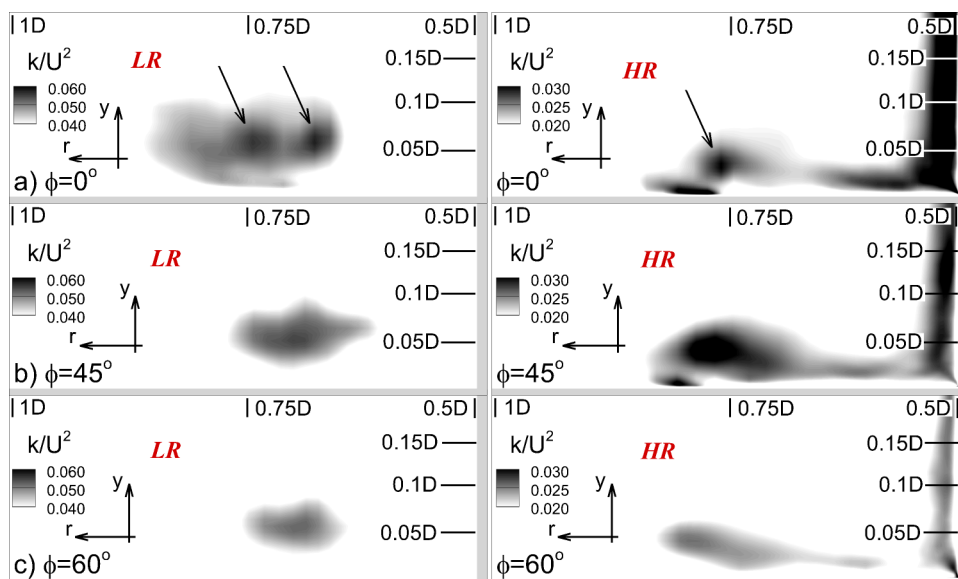

FIG. 6. Resolved turbulent kinetic energy, k/U^2, in case LR (left) and case HR (right) simulations. (a) $\phi = 0°$; (b) $\phi = 45°$; (c) $\phi = 60°$. The upstream face of the cylinder is situated at $r = 0.5D$. Values of k/U^2 less than 0.04 for case LR and less than 0.02 for case HR were blanked out.

in case HR the core of PV is situated closer to the bed, strong ejections of patches of vorticity of opposite sign to the vorticity inside PV are observed within the region where the jet-like flow detaches from the bed (r ≈ 0.8D for |φ| < 45°). As a result, the tke amplification relative to the peak tke values within the core of PV is significantly larger in case HR within the near-bed region where the jet-like flow detaches from the bed (x ≈ 0.75D-0.8D, see Figs. 6(a) and 6(b) for case HR). The measurements of Devenport and Simpson[8] also showed a large amplification of the tke in the symmetry plane inside the region where the jet-like flow detaches from the bed.[28] The average values of the nondimensional Reynolds stresses within the region corresponding to the core of PV in the mean flow are generally 50%-100% larger in case LR (e.g., see Fig. 5 for $\overline{v'v'}/U^2$, note the different contour level scales used for cases LR and HR).

Another interesting feature of the distribution of $\overline{v'v'}$ in Fig. 5 is the presence of two relative maxima within the HV region, at least for small values of |φ|. In case LR, the values associated with the two relative maxima (≈0.055U²) are comparable in the |φ| = 0° section (Fig. 5(a)). In the |φ| = 45° and |φ| = 60° sections, the peak closer to the cylinder is characterized by a larger value of the normal stress. The two relative maxima are associated with the zero flow mode and the back flow mode. These results for case LR suggest that while PV spends an approximately equal amount of time in the two modes in the φ = 0° section, the zero flow mode starts dominating as one moves away from the symmetry plane. The two peak distribution is not observed for |φ| > 70° for case LR (not shown). The distributions of $\overline{v'v'}$ for case HR (Fig. 5) show the presence of two relative maxima in the φ = 0° and φ = 45° sections. However, as opposed to case LR, the largest amplification of $\overline{v'v'}$ occurs in the region associated with the back flow mode rather than the zero flow mode.

In case LR, the trends observed in the tke distribution within the HV region in Fig. 6 are qualitatively similar to those observed for $\overline{v'v'}$. By contrast, only one relative maximum is present in the distribution of the tke within the core of PV in the symmetry plane in case HR. As will be discussed in Sec. III D, this does not mean that the core of PV is not subject to bimodal oscillations in case HR.

2. Turbulence production

Besides amplifying the turbulent stresses, the bimodal oscillations of PV induce regions where the turbulence production is high. Figures 7(a) and 7(b) provide a comparison of the nondimensional distributions of the production term in the turbulent kinetic energy equation, $P_k D/U^3$, in the symmetry plane predicted by LES in case LR with those measured by Devenport and Simpson.[8] Despite the fairly large difference in the Reynolds number (16 000 vs. 125 000) and shape of the cylinder, the distributions of $P_k D/U^3$ present many similarities. The fairly good level of agreement
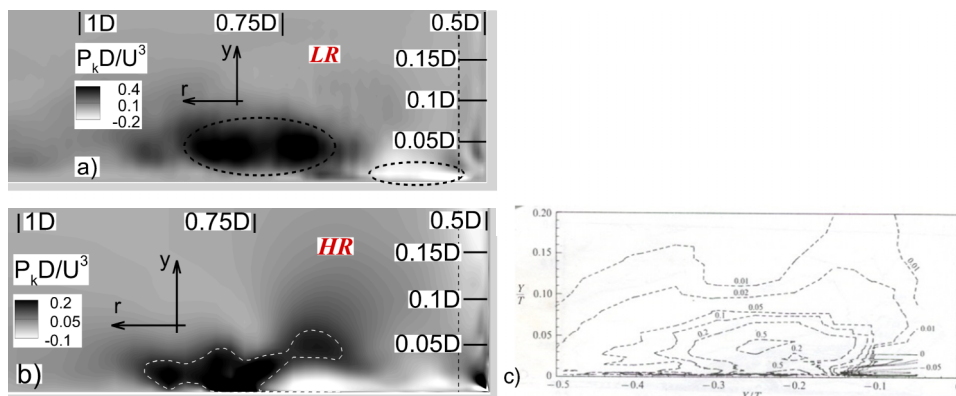

FIG. 7. Total production term in the transport equation for the turbulent kinetic energy, φ = 0° plane. (a) case LR; (b) case HR; (c) experiment conducted for Re_D = 125 000 by Devenport and Simpson.[8] No experimental data were measured in between the upstream face of the cylinder (r = 0.5D) and the dashed line shown in frames (a) and (b). Frame c is reproduced with permission from Devenport and Simpson, J. Fluid Mech. **210**, 23–55 (1990). Copyright 1990 Cambridge University Press.

is mainly because the shape of the upstream part of the cylindrical obstruction used in the experiments of Devenport and Simpson[8] was close to that of a circular cylinder and the thickness of the incoming boundary layer at the location of the wing-shaped cylinder was comparable to the width/diameter of the cylinder. In case LR, LES predicts the formation of an elongated region of large turbulence production containing two relative maxima associated with the two modes. The region of high P_k induced by the bimodal oscillations of PV extends between 0.2D and 0.4D from the face of the circular cylinder in case LR. Note that the threshold value of $P_k D/U^3$ used to identify the region of high P_k is 0.15. The same region extends between 0.15D and 0.35D from the upstream face of the wing-shaped cylinder. The main difference is the shape of this region, which is elliptical in case LR and mushroom-like in the experiment and case HR. The LES of case LR and the experiment predicts the formation of a near-bed region of high negative turbulence production for $0.53 < r/D < 0.65$.

Comparison of the distributions of P_k in the $|\phi| = 0°$ plane (Figs. 7(a) and 7(b)) shows that as Re_D increases, the near-bed patch of negative P_k values becomes thinner and penetrates beneath the large region of high positive P_k. This feature of the distribution of P_k in case HR is similar to what was observed in the $Re_D = 125\,000$ experiment (Fig. 7(c)) and is mainly due to the increase in the energy content of the eddies advected within the downflow and the jet-like flow with Re_D. The region for which $P_k D/U^3 > 0.15$ has a mushroom-like shape in case HR, which is qualitatively very similar to the distribution of P_k given by experiment. This is because the core of PV gets closer to the bed as the Reynolds number increases. Moreover, the peak values of $P_k D/U^3$ are close to 0.55 and are situated at a distance of around 0.025D from the cylinder in case HR and experiment. The peak values of $P_k D/U^3$ are around 0.7 in case LR (note that the maximum iso-contour value represented in Figs. 7(a) and 7(b) is less than the peak value).

The good agreement between the distribution of P_k predicted by present simulations and the experiment of Devenport and Simpson[8] is an important success of the present simulations, given that previous numerical investigations using steady inflow conditions failed to correctly predict the location of the core of PV and of the associated regions of high tke and P_k with respect to the cylinder (e.g., Paik et al.[28]). Another difference with such investigations was that no secondary hairpin vortices developed on the core of PV as a result of the interaction of PV with an approaching secondary necklace vortex. Again, this difference is due to the presence of resolved fluctuations in the incoming flow (see discussion in Chang et al.,[50] on the conditions needed for hairpin-like vortices to be induced on the core of a large vortex by neighboring vortices), which is physically more correct and consistent with conditions present in the experiments and in the field.

3. Effect of cylinder shape

The effect of the cylinder shape on the turbulence amplification within the HV region is discussed next. Figure 8 shows the tke distribution within the HV region for the case of a high aspect ratio rectangular cylinder of width equal to that of the circular cylinder in case HR at a comparable cylinder Reynolds number ($Re_D = 2.4 * 10^5$, Kirkil[41]). The ratio between the cylinder width and the channel depth and the ratio between the cylinder width and the channel width were identical to the corresponding values in case HR.
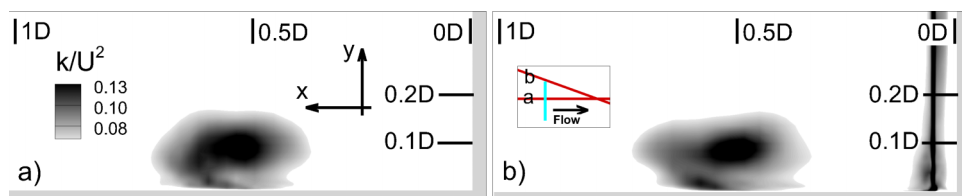

FIG. 8. Resolved turbulent kinetic energy, k/U^2, for the flow past a high-aspect-ratio rectangular cylinder at $Re_D = 2.4 * 10^5$ (Kirkil[41]). Results are shown in the symmetry plane of the cylinder (a) and in a plane cutting through the edge of the cylinder (b), as shown in the inset in frame (b). The upstream face of the rectangular cylinder is situated at $x/D = 0$. Values of k/U^2 less than 0.07 were blanked out.
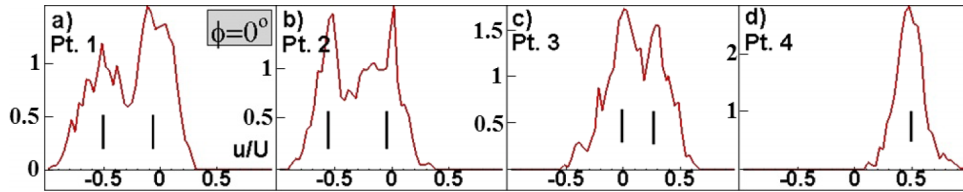
FIG. 9. Histograms of probability density function of radial velocity showing normalized frequency vs. radial velocity along a vertical line cutting the HV region in the $\phi = 0°$ plane (see Fig. 5(a)) at (a) point 1; (b) point 2; (c) point 3; (d) point 4. Results are shown for case LR.

Comparison of the tke in Figs. 6(a) and 6(b) (case HR) and Figs. 7(a) and 7(b) shows that the average amplification of the tke within the HV region is about 4 times larger in the case of a rectangular cylinder, the core of the PV is larger and situated farther away from the upstream face of the cylinder (e.g., at 0.5D for the rectangular cylinder and at 0.25D for the circular cylinder in the symmetry plane). These results also show that for blunt cylinders, the large amplification of the tke within the region where the jet-like flow detaches from the bed (e.g., see Figs. 6(a) and 6(b) for case HR and Fig. 8(b)) is a general characteristic of the turbulence structure within the HV system at high Reynolds numbers regardless of the shape of the cylinder.

D. Velocity histograms and power spectra

Analysis of the histograms of the probability density function of the velocity components allows determining the extent of the region where bimodal oscillations are present. Several probability density functions (pdf's) are plotted for case LR in Figs. 9-11. The pdf's are analyzed along a vertical line cutting through the middle of the core of PV in the mean flow. The pdf's of the radial velocity (streamwise velocity in the $|\phi| = 0°$ plane) in Fig. 9 display a double-peak shape, indicating the presence of bimodal oscillations starting very close to the bed (e.g., point 1 in Fig. 5(a) situated within the jet-like flow) and inside the region of high amplification of the turbulent stresses (e.g., points 2 and 3). However, the pdf's of the radial velocity reverse to a standard one-peak shape above the core of PV (e.g., point 4). As shown in Fig. 10, none of the pdf's of the polar velocity (spanwise velocity in the $|\phi| = 0°$ plane) display a two-peak shape within or below the core of PV (the small oscillation near the maximum pdf values in Fig. 10(c) resembling a double-peak shape is due to the finite length of the velocity time series). This is expected, as the bimodal oscillations do not induce large-scale fluid movement along the axis of PV.

The histograms of the radial and vertical velocities in the $|\phi| = 45°$ plane (e.g., several pdf's of the radial velocity are shown in Fig. 11) also contain two peaks at points situated within the core of PV, but one of the peaks is higher and has a wider base (always the peak corresponding to the zero flow mode) compared to the other peak. All the histograms of the vertical and radial velocities displayed a one-peak shape within the HV region for $|\phi| > 70°$, which confirms that the legs of PV are not subject to bimodal oscillations and the strength of the bimodal oscillations is the largest in the region where the obstacle induces strong adverse pressure gradients in the radial direction. This is also why bimodal oscillations induced by a rectangular cylinder or by a plate of equal width to that of a circular cylinder are significantly stronger than those observed in front of
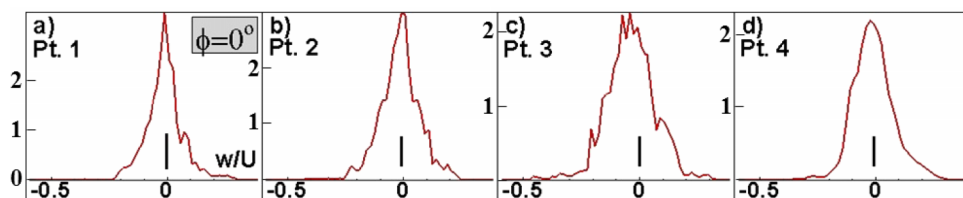

FIG. 10. Histograms of probability density function of polar velocity showing normalized frequency vs. radial velocity along a vertical line cutting the HV region in the $\phi = 0°$ plane (see Fig. 5(a)) at (a) point 1; (b) point 2; (c) point 3; (d) point 4. Results are shown for case LR.
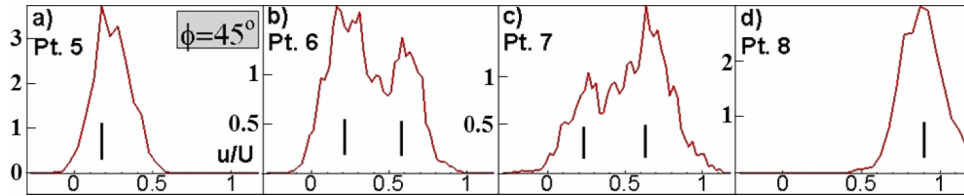
FIG. 11. Histograms of probability density function of radial velocity showing normalized frequency vs. radial velocity along a vertical line cutting the HV region in the $\phi = 45°$ plane (see Fig. 5(b)) at (a) point 5; (b) point 6; (c) point 7; (d) point 8. Results are shown for case LR.

a circular cylinder (see also Chang *et al.*,[29] Kirkil[41]). Velocity histograms for case HR also confirm the presence of bimodal oscillations of the core of PV (e.g., see sample pdf's for the radial velocity showing a two-peak shape in Fig. 12).

The time intervals corresponding to successive mode switching were computed at several points inside the bimodal region (not shown). The mean residence time was estimated to be t = 2.66D/U for case LR. However, the residence time varied between about 1D/U and 6.5D/U, confirming the aperiodic nature of the large-scale oscillations of PV. Velocity spectra calculated at points situated within the region where bimodal oscillations are strong contained a range of energetic frequencies between St = 0.07 and St = 0.65 (Fig. 13), where St = fD/U is the Strouhal number corresponding to a frequency f. The mean residence time corresponds to St ~ 0.18, as one full oscillation has a mean period of 2 ∗ 2.66D/U = 5.32D/U. The lowest energetic frequency in Fig. 13 (St = 0.07) is induced by switching events with a larger residence time (t ≅ 6.5D/U). Additional analysis of the instantaneous flow fields showed that the shedding of secondary necklace vortices from the separation region occurs at somewhat higher frequencies, 0.29 < St < 0.8. The predicted range of energetic frequencies for case LR is comparable to that inferred from experiments[2,12] conducted for circular and rectangular cylinders at comparable Re_D. A similar analysis done for case HR (not shown) showed that the mean value of the residence time of PV in one mode is lower by about 30% compared to case LR.

E. Dynamics of the legs of the necklace vortices

The dynamics of the legs of the necklace vortices are qualitatively similar in cases LR and HR. The temporal snapshots of the in-plane vorticity contours in Fig. 14 (case LR) reveal an interesting mechanism for bed erosion, which is a main contributor to the growth of the scour hole on the sides of the cylinder in the case of a loose bed. At most times, the legs of PV are oriented at a small angle with the streamwise direction. However, at times, the downstream end of one of the legs of PV bends toward the symmetry plane, $\phi = 180°$ (Fig. 14(b)), and is then advected laterally (Fig. 14(b)), away from the cylinder and the symmetry plane, as it separates from the leg (Fig. 14(c)). Sometimes, several vortical streaks detach from the end of one of the legs (e.g., streaks A and B in Fig. 14) in a quick succession. The angle between the streaks and the streamwise direction is generally in the range of 15°–45°. Most of these streaks maintain their coherence over 1D/U-3D/U. As the
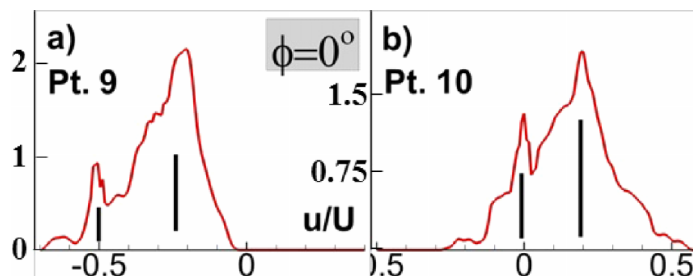

FIG. 12. Histograms of probability density function of radial velocity showing normalized frequency vs. radial velocity along a vertical line cutting the HV region in the $\phi = 0°$ plane (see Fig. 5(a)) at (a) point 9; (b) point 10. Results are shown for case HR.
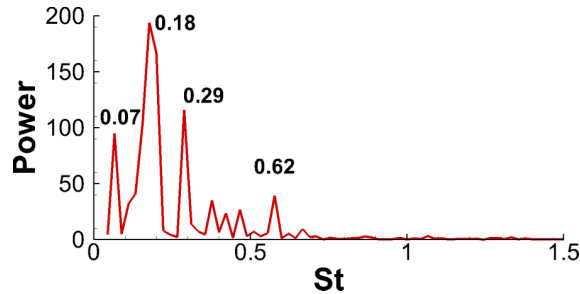
FIG. 13. Radial velocity power spectrum at point 3 (Fig. 5(a)) situated in the $\phi = 0°$ plane (case LR).

axis of these vortical streaks remains parallel to the bed, these eddies can significantly amplify the local bed shear stress before they dissipate (not shown).

Though we did not include figures to illustrate them, examination of the instantaneous flow fields for cases LR and HR has revealed other types of interactions between the PV and the SSL eddies. In both cases, at times, one of the legs of the PV approaches the SSL. When this happens, larger-scale eddies from the recirculation region at the back of the cylinder can extract vorticity from the leg of PV and increase their coherence close to the bed. As a result, these eddies increase their capacity to entrain sediment from the back of the cylinder and transport it downstream toward the location where a mount of deposited sediment forms in the case a circular cylinder is placed on a loose bed.[30] Strong interactions were also observed in case HR between the legs of PV and the downstream part of the SSLs at time instances where the coherence of PV on one side of the cylinder is large.

IV. SEPARATED SHEAR LAYERS AND NEAR WAKE REGION

A. General features of the mean flow and vortical flow structures behind the cylinder

The mean flow streamline patterns at the free surface are visualized in Fig. 15(a) for case LR. Comparison with LSPIV measurements (Fig. 15(b)) conducted for the flow conditions corresponding to case LR ($Re_D = 16\,000$) shows that LES accurately captures the position and size of the core of the two vortical eddies behind the cylinder which define the recirculation bubble. The size of the recirculation bubble is $(x_v, z_v) = (2.14D, 1.35D)$ in experiment and $(2.28D, 1.28D)$ in the simulation.
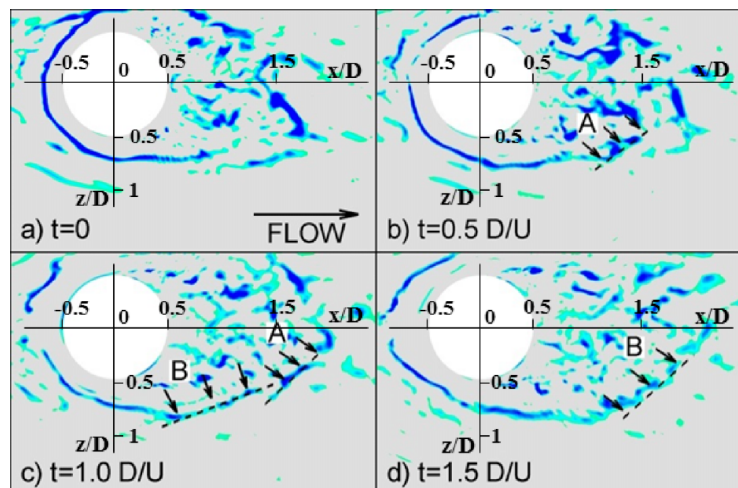

FIG. 14. Visualization of the dynamics of the legs of the primary necklace vortex, PV (case LR). The four frames show in-plane vorticity magnitude contours in the $y/D = 0.04$ plane at successive time instances. The figure illustrates the detachment of streaks of rotational fluid from the legs of PV that are then advected parallel to the bed and away from the symmetry axis.
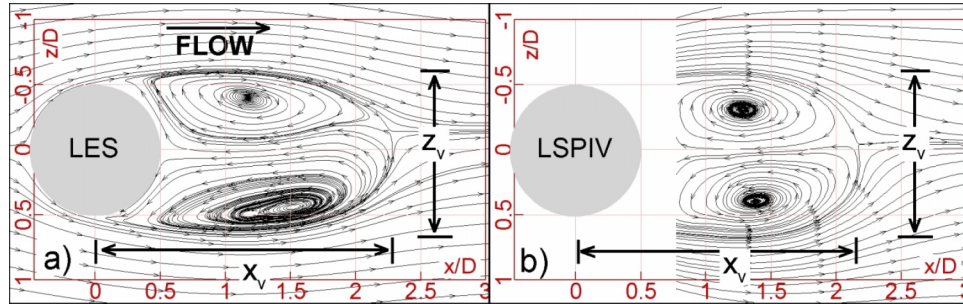
FIG. 15. Mean 2-D streamline patterns at the free surface in the region situated behind the cylinder (case LR). (a) LES; (b) LSPIV.

The cylinder drag coefficient calculated with the total (pressure and friction) mean force acting in the streamwise direction and with the incoming flow velocity at the free surface was estimated as $C_D = 1.06$. This value is close to experimental measurements reported in the literature for long circular cylinders ($C_D \cong 1.1$-1.2) and for finite length cylinders ($C_D \cong 1.03$) as well as with LES and DES conducted at subcritical Reynolds numbers.[46,47]

Figure 16(a) visualizes one of these vortical eddies using 3-D streamlines. The two eddies resemble tornado-like vortices that draw fluid particles toward the free surface. However, not all fluid particles are entrained from near the bed. Part of the fluid particles is originating from a spanwise oriented vortex situated close to the cylinder. The vortex is visualized in Fig. 16(a) using 2-D streamlines in the symmetry plane $\phi = 180°$. Fluid particles situated near the symmetry plane and close to the bed are first entrained into the core of the spanwise-oriented vortex and from there toward the free surface by the two tornado-like vortices. The presence of such a spanwise oriented vortex is confirmed by dye visualizations (Fig. 16(a)) conducted by Akilli and Rockwell[20] at a similar Reynolds number ($Re_D = 20\,104$) but for a shallower case ($H/D = 0.5$ compared to $H/D = 1.12$ for case LR). In the case of a loose-bed, this vortex together with the upwelling motions within the two tornado-like vortices plays an important role in the transport of sediment particles entrained from the bed close to the back of the cylinder. The general flow pattern illustrated by the streamlines in Fig. 16(a) is also similar to the mean flow predicted by the Reynolds Averaged Navier Stokes (RANS) simulations of Zhao *et al.*[43] of flow past circular piers.

Figure 16(b) shows the near-bed flow topology for case LR. Two saddle points and two foci points are present. Despite the differences in H/D, the flow topologies in case LR and in the experiment of Akilli and Rockwell[20] are very similar (Fig. 16(b)). 3-D streamlines launched very close to the bed
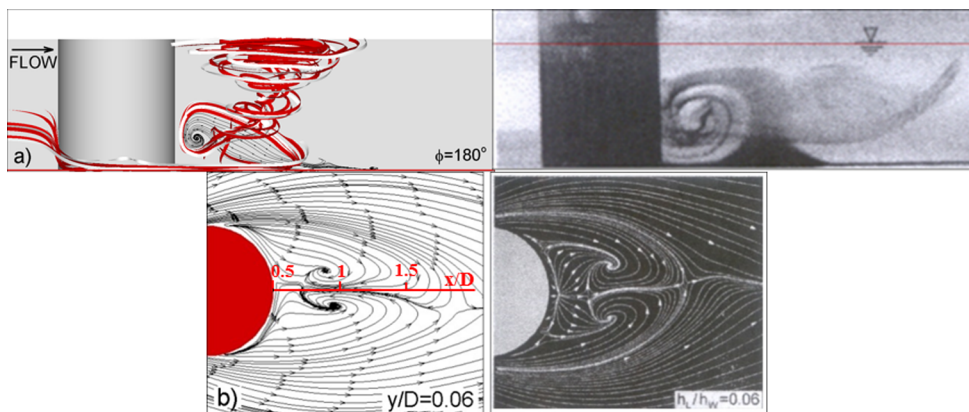

FIG. 16. Mean flow structure behind the cylinder. (a) Side view in the $\phi = 180°$ plane; (b) 2-D streamline patterns in the $y/D = 0.06$ plane. Left frames show results for case LR. Right frames show experimental results of Akilli and Rockwell[20] obtained for $Re_D = 20\,052$. Experimental results are reproduced with permission from Akilli and Rockwell, Phys. Fluids **14**(9), 2957–2967 (2002). Copyright 2002 AIP Publishing.
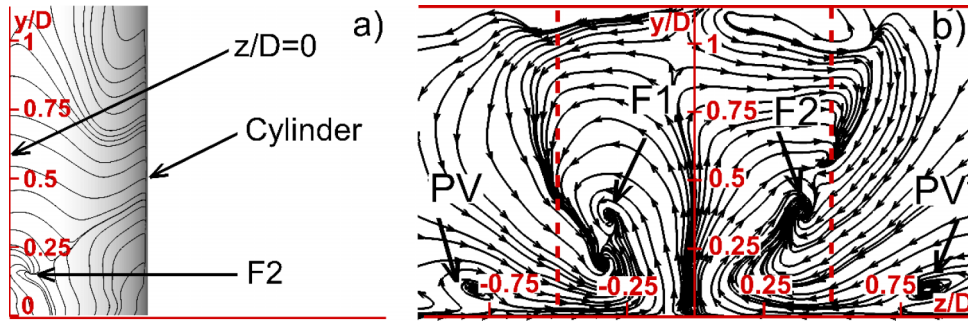
FIG. 17. Mean flow structure behind the cylinder for case LR. (a) 2-D limiting streamlines on the cylinder surface showing foci point where one of the two counter-rotating vortices is attaching to the cylinder. (b) 2-D streamlines in x/D = 1 plane showing the two counter-rotating vortices and the legs of the primary necklace vortex, PV. The vertical dashed lines show the projection of the cylinder on the x/D = 1 plane.

at the location of the two foci points were entrained into the two tornado-like vortices (not shown). This means that the two foci points correspond to the locations where the axes of the tornado-like vortices attach to the bed.

The 2-D mean flow streamline patterns in Fig. 17(b) show that besides the legs of PV, which are situated at about 0.8D from the symmetry plane, two foci points corresponding to a pair of counter-rotating vortical eddies are present in the x/D = 1 plane. The upwelling flow motions close to the symmetry plane are compensated by downwelling flow motions on the outside of the recirculation bubble. The predicted flow topology in spanwise-vertical (x = constant) planes cutting through the recirculation region is in good qualitative agreement with the topology inferred from experiments conducted at Re_D = 7000 by Sahin and Ozturk[18] in a much deeper channel (H/D = 6.0). Their experiments also captured the pair of foci points situated close to the symmetry plane. However, previous experimental investigations were not able to locate where the two eddies originate. Numerical results for case LR show that the two counter-rotating eddies attach to the back of the cylinder, close to the symmetry plane (Fig. 17(a)). The axes of the two eddies are close to parallel to the bed and situated at 0.2D-0.4D from it. Thus, these vortical eddies can play an important role in the transport of entrained sediment away from the back of the cylinder in the case of a loose bed.

B. Reynolds number effects on the flow structure behind the cylinder

1. Eddy content of the SSLs

Due to the drag crisis which moves the separation line downstream, the value of the streamwise drag coefficient estimated at the free surface for case HR (C_D = 0.53) was significantly lower compared to case LR (C_D = 1.06). However, this value is close to values obtained from experiments ($C_D \approx 0.4$) and DES (C_D = 0.57-0.59) of flow past long circular cylinders in the supercritical regime, at comparable cylinder Reynolds numbers.[46–48]

Several important differences are observed in the shape and dynamics of the vortex tubes shed in the SSLs between case LR (Fig. 18(a)) and case HR (Fig. 18(b)). In case LR, the flow is laminar within the upstream part of the SSLs. The first couple of vortex tubes extends over the whole flow depth, even though large deformations of their cores with respect to the vertical direction are observed. Examination of the instantaneous flow fields shows that merging of successively shed vortex tubes occurs over the upstream part of the SSLs. However, because of the strong deformations of the axes of the vortex tubes, the merging between the cores of two vortex tubes occurs over a limited distance. Once the SSLs become turbulent, the stretching of the vortex tubes is very severe and vortex breakdown occurs. As a result, the tubes lose their coherence and small scale turbulence is generated. The turbulent eddies in the fully turbulent incoming flow are the main reason why the shedding frequency of the vortex tubes in the SSLs is not constant. Rather, the range of frequencies at which vortex tubes are shed varies between St = 2.5 and St = 4 (not shown). In average, one merging event occurs in
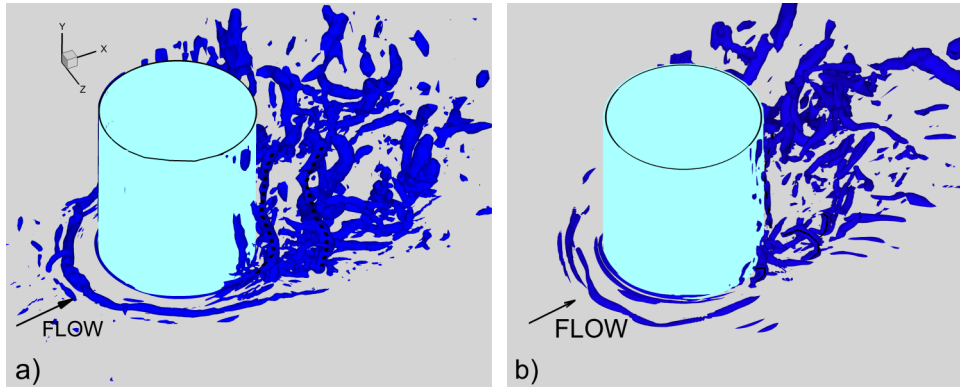
FIG. 18. Large scale coherent structures in an instantaneous flow field visualized using the Q criterion. (a) Case LR; (b) case HR. In case LR, the deformed vortex tubes extend from the bed to the free surface. In case HR, the coherence of the vortex tubes is rapidly lost and hairpin like eddies are present in the vicinity of the bed.

the SSL before transition to turbulence starts. This explains why velocity power spectra calculated at points situated within the turbulent part of the SSLs contain a range of energetic frequencies between $St = 1.2$ and $St = 4$ (e.g., see Fig. 19(a)).

Compared to case LR, the cores of the vortex tubes in case HR are strongly deformed away from the free surface starting in the region they form. Only the core of the first vortex tube in Fig. 18(b) maintains its coherence over most of the flow depth and its axis remains close to parallel to the vertical direction away from the bed. Due to the large variation of the angle at which the attached boundary layer separates close to the bed, the initial orientation of the vortex tubes close to the bed surface is not along the vertical direction. This is also why the cores of the vortex tubes are rapidly distorted in the near bed region. Analysis of the instantaneous flow fields shows that the bottom parts of most of the vortex tubes reorient themselves along a direction that makes a low angle with the bed. The rate of growth of the 3D instabilities inside the SSLs is larger in case HR.

Examination of the instantaneous flow fields in case HR also shows the presence of hairpin eddies at the interface between the high-speed flow on the two sides of the cylinder and the low-speed recirculating flow behind the cylinder (e.g., such eddies are visible in Fig. 18(b) on the right side of the cylinder). Most hairpins form on the outer side of the SSLs.

2. Large scale vortex shedding in the wake

The dominant frequency of the velocity components within the near wake corresponds to $St = 0.26$ in case LR (Fig. 19(b)) and to $St = 0.27$ in case HR. The mechanisms responsible for the formation of roller vortices behind the cylinder and their shedding are very similar in both cases. Each roller forms as a result of the movement of one of the SSLs toward the symmetry plane, which favors the
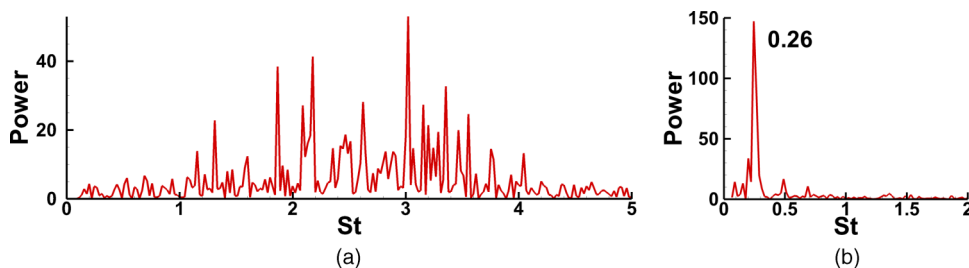

FIG. 19. Power spectra (right) of the spanwise velocity, w/U (case LR). (a) Point located inside one of the SSLs (the coordinates of the point are $x = 0.8D$, $y = 0.9D$, and $z = 0.65D$); (b) point located inside the near wake (the coordinates of the point are $x = 5.0D$, $y = 0.9D$, and $z = 0.0D$).
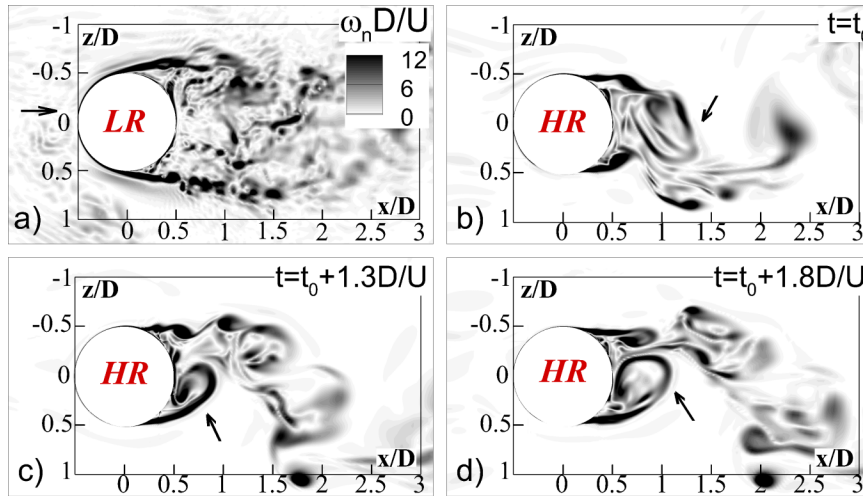
FIG. 20. Vertical vorticity magnitude, $\omega_y(D/U)$ at $y/D = 1$ in the instantaneous flow. (a) Case LR, (b)-(d) case HR. The arrows in frames (b)-(d) point toward the roller vortices forming behind the cylinder.

accumulation and merging of eddies shed in the other SSL into a larger (roller) vortex. Once the circulation of the new roller becomes sufficiently large, the roller starts moving away from the cylinder. This process is illustrated in Figs. 20(b)-20(d) for case HR. Figure 20(b) shows a roller containing negative vorticity when it starts moving away from the back of the cylinder (left side relative to the incoming flow direction). As this happens, a new roller containing positive vorticity forms behind the cylinder (Fig. 20(c)). The new roller starts detaching from the cylinder in Fig. 20(d).

Analysis of the instantaneous flow fields shows that the average diameter of the roller vortices decreases and their degree of coherence (e.g., as measured by the vertical circulation) grows significantly as Re_D increases above values at which the drag crisis occurs on the cylinder. Comparison of the vorticity fields in Fig. 20(a) (case LR) and Fig. 20(c) (case HR) shows that the eddies containing positive vorticity which are part of the core of the new roller forming on the right side of the cylinder are more energetic and occupy a larger percentage of its core in case HR. Moreover, while the new roller vortices never penetrate at less than 0.5D from the back of the cylinder in case LR (Fig. 20(a)), they are impinging on the back of the cylinder in case HR (Figs. 20(b) and 20(c)). A main reason for these quantitative changes in the structure of the rollers is the decrease in the length of the SSLs and of the spanwise distance between the SSLs once the drag crisis occurs. As the roller vortices form closer to the cylinder and are more coherent when supercritical flow conditions are present, it is expected that their capacity to entrain and transport sediment from the back of the cylinder will be larger in case HR compared to case LR.

C. Vertical nonuniformity of near wake flow and Reynolds number effects

Away from the bed ($y/D > 0.4$), the SSLs separate at $\phi_s = 84°$ in case LR (Figs. 21(a) and 21(b)). As the bed is approached, ϕ_s increases to 88° (Fig. 21(c)). A similar trend was observed in the experiment conducted by Dargahi[2] for $Re_D = 39\,000$. The average separation angle was close to 85° and its values were larger in the near-bed region. Results for case HR show that, as a result of the drag crisis, ϕ_s increases to 108° away from the bed. However, very close to the bed the flow separates at around 90°, which is a direct consequence of the fact that the cylinder Reynolds number defined with the mean incoming streamwise velocity close to the bed eventually decreases below the threshold value at which the drag crisis occurs. For example, $\phi_s = 95°$ at $y/D = 0.1$ in Fig. 21(c). As a result of the drag crisis, the length of the recirculation region behind the cylinder reduces from 2.28D in case LR to 1.25D in case HR close to the free surface. The length of the recirculation bubble inferred from LSPIV measurements conducted for case HR was 1.20D. Because of the earlier separation occurring
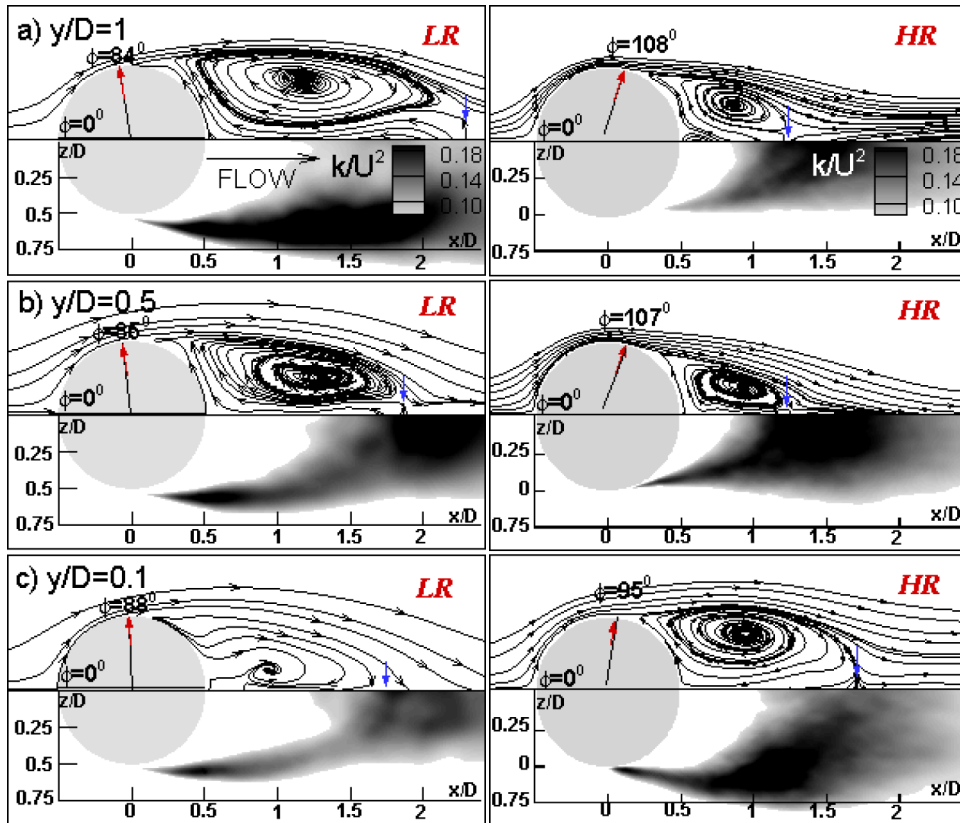
FIG. 21. Turbulent kinetic energy, k/U^2, and 2-D streamline patterns in horizontal planes for case LR (left) and case HR (right). (a) $y/D = 1$; (b) $y/D = 0.5$; (c) $y/D = 0.1$. The arrows indicate the position of the separation line on the cylinder. The vertical arrows indicate the end of the recirculation bubble. Values of k/U^2 less than 0.08 were blanked out.

in the bed vicinity, the length of the recirculation region in case HR increases to 1.7D close to the bed.

The distributions of the resolved tke in Fig. 21 show that, with the exception of the near-bed region, the region of high k/U^2 induced by the lateral movement of the ends of the SSLs is larger in case HR. This region is centered around $x/D = 2$ for case LR and $x/D = 1.5$ for case HR (Figs. 21(a) and 21(b)). Meanwhile, the largest differences occur within the upstream part of the SSLs where, away from the bed, the nondimensional tke levels in case LR are much higher than those predicted in case HR. However, these differences are very small in the near bed region (Fig. 21(c)), where the flow is subcritical in both simulations (e.g., at $y/D = 0.1$).

The orientation of the SSLs in case LR is vertically close to the free surface. Away from the free surface, the SSLs bend slightly toward the symmetry plane (Fig. 22(a)). As one moves downstream, the tilting angle between the surface bordering the near wake region and the outer flow with the vertical increases from about 5° at $x/D = 0.5$ to about 25° at $x/D = 2$ (Fig. 22(a)). In case HR (Fig. 22(b)), the vertical variation in the position of the SSLs is different. As one moves away from the free surface, the SSLs get closer to each other until $y/D = 0.6$ and then move away from each other until the bed surface. This trend is consistent with the decrease in ϕ_s and the increase of the size of the recirculation bubble as the bed surface is approached (Fig. 21). In case HR, the highest amplification of the tke within the SSLs occurs over the lower half of the flow depth (Fig. 22(b)). As one moves downstream, the average tilting angle of the surface bordering the near wake region decreases. While in case LR, the width of the near wake decreases with the distance from the free surface, the opposite is true for case HR. However, the average level of amplification of the nondimensional tke within the SSLs and the near wake regions is comparable in the two cases.
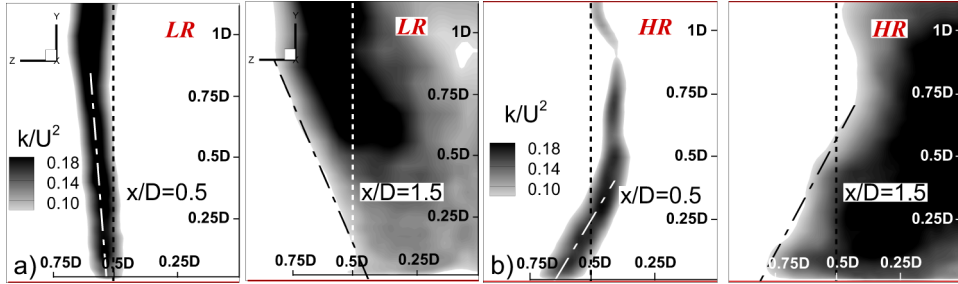
FIG. 22. Turbulent kinetic energy, k/U^2, in vertical spanwise planes. (a) Case LR; (b) case HR. Results are shown in two parallel planes, $x/D = 0.5$ and $x/D = 1.5$ (x is the streamwise direction parallel to incoming flow). The vertical dotted line denotes $z = 0.5D$. The dashed-dotted line indicates the centerline of the lower part of the SSL ($x/D = 0.5$) and the boundary between the near wake region and the external flow ($x/D = 1.5$). Values of k/U^2 less than 0.08 were blanked out.

V. BED FRICTION VELOCITY

A. Time-averaged distributions

The largest amplification of the bed friction velocity magnitude in the mean flow, $\bar{u}_\tau/u_{\tau 0}$ ($u_{\tau 0}$ is the mean bed friction velocity in the incoming fully turbulent flow away from the cylinder, $u_{\tau 0}$ decreases with the increase in the Reynolds number), occurs in the region of strong flow acceleration generated by the deflection of the incoming flow by the cylinder's surface (Fig. 23). Relatively large $\bar{u}_\tau/u_{\tau 0}$ values are also observed beneath the upstream part of the SSLs and on their outer side.

In both cases, the levels of $\bar{u}_\tau$ beneath the PV are lower by more than 50% than those recorded in the region of strong flow acceleration and within the upstream part of the SSLs. The lowest values of $\bar{u}_\tau$ beneath PV are observed for low polar angles ($|\phi| < 30°$, Fig. 23(a)). Still, even for $\phi = 0°$, the ratio $\bar{u}_\tau/u_{\tau 0}$ is larger than 1.3, which is consistent with the findings of Roulund et al.[3] The largest levels of $\bar{u}_\tau/u_{\tau 0}$ occur for $|\phi| \cong 50°$, close to the face of the cylinder. Within this region of high mean bed friction velocity, the radial variation of $\bar{u}_\tau/u_{\tau 0}$ is qualitatively similar in the two cases, but the peak values of $\bar{u}_\tau/u_{\tau 0}$ are higher in case LR (3.5) compared to case HR (2.5).

B. Temporal variability of the instantaneous flow distributions and their effect on the root-mean-square (rms) of the bed friction velocity

Despite the large differences observed in the mean flow, at times, the values of the instantaneous bed friction velocity magnitude, u_τ, beneath the core of PV and/or the cores of some of the secondary necklace vortices become comparable to the u_τ values within the region of strong flow acceleration generated by the deflection of the incoming flow by the obstacle (e.g., see Fig. 25 for case HR). This generally happens when the axis of a necklace vortex approaches the bed surface and its coherence
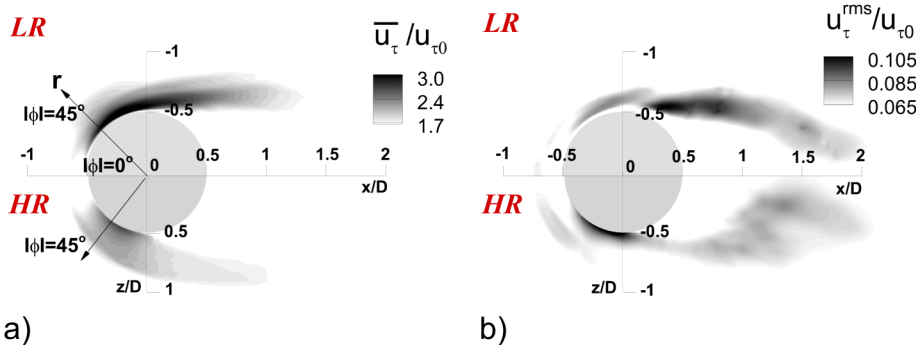

FIG. 23. Mean bed friction velocity, $\bar{u}_\tau/u_{\tau 0}$ (left), and mean rms fluctuations of the bed friction velocity, $u_\tau^{rms}/u_{\tau 0}$ (right), in case LR (top) and case HR (bottom).

increases via one of the previously described mechanisms. Thus, even for flat-bed conditions, the erosion capacity of the HV system is not negligible. These findings are consistent with results of previous experimental investigations of local scour around circular cylinders under clear water scour conditions.[2,23,43]

The presence of energetic necklace vortices in the vicinity of the bed and the advection of large-scale eddies over the bed surface situated beneath the SSLs and near wake are the main reasons for the presence of regions of high rms fluctuations of the bed friction velocity magnitude, $u_\tau^{rms}/u_{\tau0}$, in the vicinity of the cylinder (Fig. 23(b)). In both cases, the regions of high u_τ^{rms} do not coincide with those of high $\bar{u}_\tau$ (Fig. 23(a)). This can have important consequences for local scour, as significant sediment entrainment can occur over time even in regions of high u_τ^{rms} even if $\bar{u}_\tau$ is below the critical threshold value for sediment entrainment. A classical example is the quasi-regular passage of vortex tubes or roller vortices over a certain bed location which can increase u_τ significantly with respect to $\bar{u}_\tau$. If these vortices are sufficiently large and their advection velocity is sufficiently low such that the amplification of u_τ lasts over a relatively long time interval, then a high probability for entrainment of sediment particles at that location is expected.[49]

The largest amplification of u_τ^{rms} in case LR (Fig. 23(b)) is observed over the downstream part of the SSLs which contain strongly coherent vortex tubes (Fig. 18(a)). The largest amplification of u_τ^{rms} in case HR (Fig. 23(b)) is observed in the region where the newly formed rollers start moving away from the cylinder. As already discussed, the coherence of these rollers is larger in case HR compared to case LR. As Re_D increases, the energy content of the eddies advected within the jet like flow increases and the distance between the axis of PV and the bed surface decreases (see also discussion in Sec. III C 1). This explains the larger relative amplification of the tke within the jet-like flow and within the region where ejections of patches of vorticity from the attached boundary layer take place (Fig. 6), and of u_τ^{rms} beneath the HV region (Fig. 23(b)) in case HR compared to case LR.

Figure 24 shows the distributions of $\bar{u}_\tau/u_{\tau0}$ and $u_\tau^{rms}/u_{\tau0}$ from a DES simulation of flow past a high-aspect-ratio rectangular cylinder[41] for which the turbulence structure within the HV region was presented in Fig. 8. Comparison with results obtained for case HR (Fig. 23) allows assessing the effect of the degree of bluntness of the cylinder on the potential for bed erosion. While the peak values of $\bar{u}_\tau/u_{\tau0}$ are comparable, the size of the region where $\bar{u}_\tau/u_{\tau0} > 1.5$ is by more than two times larger in the case of a rectangular cylinder. This is due to the larger coherence of the PV (see discussion of Fig. 8) and stronger coherence of the vortex tubes near the bed (in the case of a rectangular cylinder, the flow remains supercritical until the bed, as the separation line corresponds to the edge of the cylinder). Moreover, very large values of $u_\tau^{rms}/u_{\tau0}$ are observed at the back of the rectangular cylinder due to the large coherence of the rollers detaching from the back of the rectangular cylinder. These differences explain the much larger erosion potential of the flow around a rectangular cylinder placed on a flat bed compared to the corresponding case of a circular cylinder of same width.[41]

C. Effect of near-bed coherent structures on bed friction velocity

Figure 25 illustrates an important type of interactions between vortical eddies and the bed surface that result in a large amplification of u_τ beneath the HV region. Vortical eddies advected within the downflow change direction as they approach the bed. As they start moving away from the junction line within the jet-like flow, these eddies are severely stretched in the polar direction and can induce large
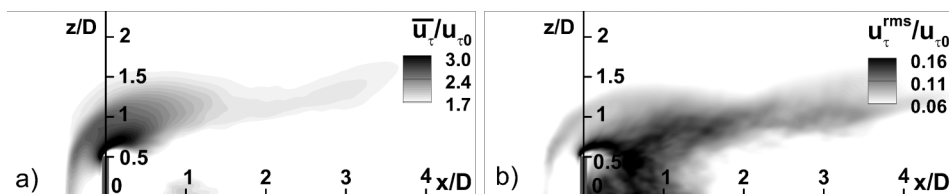

FIG. 24. Mean bed friction velocity, $\bar{u}_\tau/u_{\tau0}$ (left), and mean rms fluctuations of the bed friction velocity, $u_\tau^{rms}/u_{\tau0}$ (right), for the flow past a high-aspect-ratio rectangular cylinder at $Re_D = 2.4*10^5$. The cylinder is shown as a dark grey rectangle ($|z/D| < 0.5$ at $x/D = 0.0$).
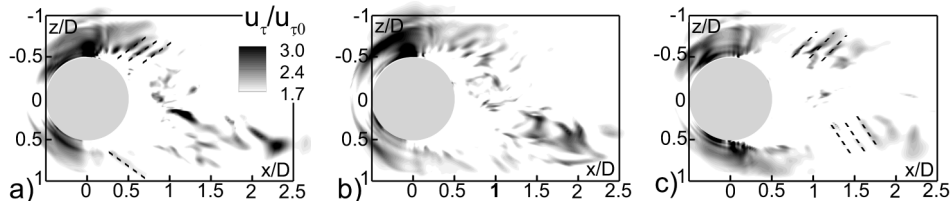
FIG. 25. Instantaneous bed friction velocity, $u_\tau/u_{\tau 0}$, in case HR. Besides the amplification of u_τ in the region of high flow acceleration centered around $|\phi| = 45°$, streaks of large u_τ values (see dashed lines) form in the downstream part of the SSLs. These streaks are primarily induced by the legs of hairpin-like eddies forming in the vicinity of the bed, similar to those visualized in Fig. 18(b).

values of u_τ before being injected into the core of PV. Figures 25(a) and 25(b) show the formation and migration away from the junction line of such a patch of high u_τ on the right side of the cylinder for case HR. This mechanism for the amplification of u_τ beneath the HV region is very important in case HR where the energy of the vortical eddies transported by the downflow is much larger compared to case LR.

Another interesting feature of the distributions of u_τ in case HR is the presence of streaks of relatively high u_τ inside the SSLs and on their outward side. At most times, several parallel streaks can be observed (Fig. 25(c)). Two main mechanisms are responsible for the formation of these streaks in case HR. The first one is the severe bending and stretching of the vortex tubes near the bed which can generate eddies with a strong horizontal component of the vorticity. The other mechanism is the amplification of u_τ by the lower leg of hairpin eddies forming on the outer side of the SSLs (e.g., see hairpin eddies in Fig. 18(b)). The mechanism responsible for the formation of the hairpin eddies was discussed in Sec. IV B.

VI. SUMMARY AND CONCLUSIONS

Eddy resolving simulations were used to study the physics of flow past a circular cylinder mounted on a flat bed in a channel with a fully turbulent incoming flow. The dynamics of the large-scale coherent structures and their effect on the mean flow, turbulence statistics, and bed shear stresses were investigated for two cases. In the first one (case LR), the cylinder Reynolds number, Re_D, was sufficiently low such that the attached boundary layers remained laminar at separation (subcritical flow conditions). In the second one (case HR), Re_D was sufficiently high for transition to turbulence to occur in the attached boundary layers (supercritical flow conditions away from the channel bed). Even for case HR, where the drag crisis occurred away from the bed, the flow conditions remained subcritical in the vicinity of the bed. Understanding flow structure and sediment erosion mechanisms in case HR is particularly relevant for field-scale applications in river and coastal engineering where flow past cylindrical obstructions (e.g., bridge piers) are always supercritical.

A main goal of the paper was to clarify the structure and dynamics of the HV system forming around the upstream face of the cylinder and how they change with the increase in the Reynolds number. The main findings are as follows:

1. In both cases, the HV region contained one primary necklace vortex, PV, whose core was subject to large-scale bimodal oscillations for polar angles less than 70°. The effect of the bimodal oscillations was to amplify the tke and most of the other Reynolds stresses within the region swept by the core of PV by about one order of magnitude with respect to the mean values in the incoming fully turbulent flow. No bimodal oscillations were observed in the legs of PV. While PV spent a comparable amount of time in both modes in case LR, the zero flow mode dominated in case HR.

2. The eddies advected within the downflow were much more energetic in case HR. As a result, the levels of tke amplification inside the jet-like flow forming beneath PV relative to those observed inside the core of the PV were much larger in case HR. This is generally the case for any high Reynolds number ($Re_D > 10^5$) turbulent HV system forming in front a bluff body.

3. The position and extent of the regions of high positive and negative turbulence production, P_k, within the HV system changed with Re_D. The nondimensional distribution of P_k in the symmetry plane in case HR was found to be qualitatively and even quantitatively similar to that measured by Devenport and Simpson[8] for a wing-shaped body at a comparable Reynolds number.

Experimental investigations of local scour showed that scour develops in regions where the values of $\bar{u}_\tau$ are too low for sediment to be entrained based on mean flow estimations.[4,30] Inside these regions, scour is driven by the passage of large-scale coherent structures. Analysis of the instantaneous flow fields allowed identifying several mechanisms involving the large-scale coherent structures present near the bed that can result in a significant amplification u_τ and thus in sediment entrainment. The most important mechanisms for the amplification of u_τ are as follows:

1. The detachment and advection of vortical streaks from the legs of the primary necklace vortex.
2. The interactions of the vortex tubes shed in the SSLs with the legs of the primary necklace vortex and the eddies originating in the downflow.
3. The merging of successively shed vortex tubes in the SSLs.
4. The advection of wake roller vortices.

Results obtained for a rectangular cylinder showed that the rollers play an even more important role in sediment entrainment and transport in the case of a cylinder with a sharp edge (e.g., square/rectangular cylinder, vertical plate) at high Re_D. For such cylinders, the coherence of the roller vortices does not decay significantly close to the bed because the flow regime past the cylinder will remain supercritical in the near-bed region (Chang *et al.*[29]). Finally, the larger energy content of the eddies advected with the downflow and the closer to bed position of the primary necklace vortex were identified as the main reasons for the larger amplification of the rms fluctuations of the bed friction velocity magnitude, u_τ^{rms}, beneath the HV region in case HR compared to case LR.

Another important Reynolds number effect was the large increase with Re_D in the three-dimensionality of the flow inside the SSLs and the formation of isolated, or arrays of, hairpin eddies at the interface between the SSLs and the high-speed flow on their outer side. The lower legs of these hairpin eddies have the capability to induce streaks of high u_τ as they are advected downstream. This is another mechanism for sediment entrainment near cylinders without sharp edges placed in a loose-bed channel at Re_D values above the one corresponding to the drag crisis.

Of particular interest will be to apply the present model to study flow past cylinders under very shallow conditions ($D/H > 20$) where the bottom friction greatly affects the streamwise development of the near wake and the HV system extends up to the free surface. This type of flows is particularly important for geophysical applications such as flow and sediment transport past islands.

[1] C. H. K. Williamson, "Vortex dynamics in the cylinder wake," Annu. Rev. Fluid Mech. **28**, 477–539 (1996).
[2] B. Dargahi, "The turbulent flow field around a circular cylinder," Exp. Fluids **8**, 1–12 (1989).
[3] A. Roulund, B. M. Sumer, J. Fredsoe, and J. Michelsen, "Numerical and experimental investigation of flow and scour around a circular pile," J. Fluid Mech. **534**, 351–401 (2005).
[4] J. Unger and W. H. Hager, "Downflow and horseshoe vortex characteristics of sediment embedded bridge piers," Exp. Fluids **42**, 1 (2007).
[5] A. S. W. Thomas, "The unsteady characteristics of laminar junction flow," Phys. Fluids **30**(2), 283–285 (1987).
[6] C. V. Seal, C. R. Smith, O. Akin, and D. Rockwell, "Quantitative characteristics of a laminar, unsteady necklace vortex system at a rectangular block-flat plate juncture," J. Fluid Mech. **286**, 117–135 (1995).
[7] C. V. Seal, C. R. Smith, and D. Rockwell, "Dynamics of the vorticity distribution in endwall junctions," AIAA J. **35**(6), 1041–1047 (1997).
[8] W. J. Devenport and R. L. Simpson, "Time-dependent and time-averaged turbulence structure near the nose of a wing-body junction," J. Fluid Mech. **210**, 23–55 (1990).
[9] C. J. Baker, "The turbulent horseshoe vortex," J. Wind Eng. Ind. Aerodyn. **6**, 9–23 (1980).
[10] C. J. Baker, "The oscillation of horseshoe vortex systems," J. Fluids Eng. **113**, 489–495 (1991).
[11] R. L. Simpson, "Junction flows," Annu. Rev. Fluid Mech. **33**, 415–443 (2001).

[12] Q. D. Wei, G. Chen, and X. D. Du, "An experimental study on the structure of juncture flows," J. Visualization **3**(4), 341–348 (2001).

[13] R. Ettema, G. Kirkil, and M. Muste, "Similitude of large-scale turbulence in experiments on local scour at cylinders," J. Hydraul. Eng. **132**(1), 33–40 (2006).

[14] Q. D. Wei, J. M. Wang, G. Chen, Z. B. Lu, and W. T. Bi, "Modification of junction flows by altering the section shapes of the cylinders," J. Visualization **11**(2), 115–124 (2008).

[15] C. Lin, P. H. Chiu, and S. J. Shieh, "Characteristics of horseshoe vortex system near a vertical plate-base plate juncture," Exp. Therm. Fluid Sci. **27**, 25–46 (2002).

[16] C. Lin, W. J. Lai, and K. A. Chang, "Simultaneous particle image velocimetry and laser doppler velocimetry measurements of periodical oscillatory horseshoe vortex system near square cylinder-base plate juncture," J. Eng. Mech. **129**(10), 1173–1188 (2003).

[17] K. Marakoes and J. Turner, "Vortex generation in the cross flow around a cylinder attached to an end-wall," Opt. Laser Technol. **38**(4-6), 277–285 (2006).

[18] B. Sahin and N. Ozturk, "Behaviour of flow at the junction of cylinder and base plate in deep water," Measurement **42**(2), 225–240 (2009).

[19] B. Sahin, H. Akili, C. Karakus, M. Akar, and E. Ozkul, "Qualitative and quantitative measurements of horseshoe vortex formation in the junction of horizontal and vertical plates," Measurement **43**(2), 245–254 (2010).

[20] H. Akilli and D. Rockwell, "Vortex formation from a cylinder in shallow water," Phys. Fluids **14**(9), 2957–2967 (2002).

[21] A. Kahraman, B. Sahin, and D. Rockwell, "Control of vortex formation from a vertical cylinder in shallow water: Effect of localized roughness elements," Exp. Fluids **33**(1), 54–65 (2002).

[22] H. Fu and D. Rockwell, "Shallow flow past a cylinder: Control of the near wake," J. Fluid Mech. **539**, 1–24 (2005).

[23] B. W. Melville and S. E. Coleman, *Bridge Scour* (Water Resources Publications, LLC, CO, USA, 2000).

[24] B. M. Sumer and J. Fredsoe, *The Mechanics of Scour in the Marine Environment* (World Scientific, 2002).

[25] C. C. Yeh, "The three-dimensional flow fields around square and circular cylinders mounted vertically on a flat plate," M.S. thesis (Department of Civil Engineering, National Chung-Hsing University, Taiwan, 1996).

[26] W. H. Graf and B. Yulistiyanto, "Experiments on flow around a cylinder, the velocity and vorticity fields," J. Hydraul. Res. **36**(4), 637–653 (1998).

[27] R. Balachandar, S. Ramachandran, and M. Tachie, "Characteristics of shallow turbulent near wakes at low Reynolds numbers," J. Fluids Eng. **122**, 302–311 (2000).

[28] J. Paik, C. Escauriaza, and F. Sotiropoulos, "On the bimodal dynamics of the turbulent horseshoe vortex system in a wing body junction," Phys. Fluids **19**, 045107 (2007).

[29] W. Y. Chang, G. Constantinescu, W. F. Tsai, and H. C. Lien, "Coherent structures dynamics and sediment erosion mechanisms around an in-stream rectangular cylinder at low and moderate angles of attack," Water Resour. Res. **47**, W12532, doi:10.1029/2011WR010586 (2011).

[30] G. Kirkil, S. G. Constantinescu, and R. Ettema, "Coherent structures in the flow field around a circular cylinder with scour hole," J. Hydraul. Eng. **134**, 572–587 (2008).

[31] G. Kirkil and G. Constantinescu, "The laminar necklace vortex system and wake structure in a shallow channel flow past a bottom-mounted circular cylinder," Phys. Fluids **24**, 073602 (2012).

[32] K. Mahesh, S. G. Constantinescu, and P. Moin, "A numerical method for large eddy simulation in complex geometries," J. Comput. Phys. **197**(1), 215–240 (2004).

[33] J. Frohlich and D. von Terzi, "Hybrid LES/RANS methods for simulation of turbulent flows," Prog. Aeronaut. Sci. **44**, 349–377 (2008).

[34] I. Fujita, M. Muste, and A. Kruger, "Large-scale particle image velocimetry for flow analysis in hydraulic applications," J. Hydraul. Res. **36**(3), 397–414 (1998).

[35] M. Muste, I. Fujita, and A. Hauet, "Large-scale particle image velocimetry for measurements in riverine environments," Water Resour. Res. **44**(4), W00D19, doi:10.1029/2008WR006950 (2008).

[36] M. Koken and G. Constantinescu, "An investigation of the flow and scour mechanisms around isolated spur dikes in a shallow open channel. Part I. Conditions corresponding to the initiation of the erosion and deposition process," Water Resour. Res. **44**, W08406, doi:10.1029/2007WR006489 (2008).

[37] M. Koken and G. Constantinescu, "An investigation of the flow and scour mechanisms around isolated spur dikes in a shallow open channel. Part II. Conditions corresponding to the final stages of the erosion and deposition process," Water Resour. Res. **44**, W08407, doi:10.1029/2007WR006491 (2008).

[38] P. Spalart, "Detached eddy simulation," Annu. Rev. Fluid Mech. **41**, 181–202 (2009).

[39] M. Koken, G. Constantinescu, and K. Blanckaert, "Hydrodynamic processes, sediment erosion mechanisms, and Reynolds-number-induced scale effects in an open channel bend of strong curvature with flat bathymetry," J. Geophys. Res.: Earth Surf. **118**, 2308–2324, doi:10.1002/2013JF002760 (2013).

[40] K. Chang, G. Constantinescu, and S. O. Park, "Assessment of predictive capabilities of detached eddy simulation to simulate flow and mass transport past open cavities," ASME J. Fluids Eng. **129**(11), 1372–1383 (2007).

[41] G. Kirkil, "Numerical study of flow, turbulence and scour mechanisms in the flow past cylinders on flat and scoured beds," Ph.D. thesis (Department of Civil and Environmental Engineering, University of Iowa, Iowa City, IA, 2008).

[42] Y. Dubief and F. Delcayre, "On coherent vortex identification in turbulence," J. Turbul. **1**, 011 (2000).

[43] M. Zhao, L. Cheng, and Z. Zang, "Experimental and numerical investigation of local scour around a submerged vertical circular cylinder in steady currents," Coastal Eng. **57**, 709–721 (2010).

[44] S. A. Kim, D. A. Walker, and R. L. Simpson, "Observation and measurements of flow structures in the stagnation region of a wing-body junction," VPI&SU Report No. VPI-E-91-20, Virginia Polytechnic Institute and State University, Blacksburg, VA, 1991.

[45] M. Koken and G. Constantinescu, "An investigation of the dynamics of coherent structures in a turbulent channel flow with a vertical sidewall obstruction," Phys. Fluids **21**, 085104 (2009).

[46] F. White, *Fluid Mechanics*, 5th ed. (McGraw Hill, New York, NY, 2003).

[47] R. P. Hansen and J. R. Forsythe, "Large and detached eddy simulations of a circular cylinder using unstructured grids," AIAA Paper 2003–0775, 2003.

[48] A. Travin, M. Shur, M. Strelets, and P. R. Spalart, "Detached-eddy simulations past a circular cylinder," Flow, Turbul. Combust. **63**, 293–313 (2000).

[49] A. Keshavarzy and J. Ball, "An application of image processing in the study of sediment motion," J. Hydraul. Res. **37**(4), 559–576 (2000).

[50] K. Chang, G. Constantinescu, and S. Park, "Analysis of the flow and mass transfer process for the incompressible flow past an open channel cavity with a laminar and a fully turbulent incoming boundary layer," J. Fluid Mech. **561**, 113–145 (2006).